International Journal of Hydrogen Energy 136 (2025) 731–741

Contents lists available at ScienceDirect

International Journal of Hydrogen Energy

journal homepage: www.elsevier.com/locate/he

Growth path and morphology of hydrogen-related cracks in grain-refined tempered martensitic steel produced by cyclic thermal treatment

Tingshu Chen [a,b], Yuhei Ogawa [c], Motomichi Koyama [b,*]

[a] State Key Laboratory of Performance and Structural Safety of Petroleum Tubular Goods and Equipment Materials, CNPC Tubular Goods Research Institute, Xi'an, 710077, China
[b] Institute for Materials Research, Tohoku University, 2-1-1 Katahira, Aoba-ku, Sendai, 980-8577, Japan
[c] Research Center for Structural Materials, National Institute for Materials Science (NIMS), 1-2-1 Sengen, Tsukuba, 305-0047, Japan

ARTICLE INFO

Handling Editor: Ibrahim Dincer

Keywords:
Hydrogen embrittlement
Martensitic steel
Cyclic heat treatment
Grain refinement
Crack tip blunting

ABSTRACT

This study investigated the effect of cyclic heat treatment on the resistance of tempered martensitic steels to hydrogen embrittlement. The cyclic heat treatment not only refined the prior austenite grain sizes from approximately 30 to 5 μm but also reduced the initial dislocation density. The change in microstructure by the cyclic heat treatment did not result in obvious differences in the mechanical properties compared with those of simple quenched and tempered steel when hydrogen was not introduced into the specimens. Hydrogen charging caused intergranular and quasi-cleavage cracking, and both cracking modes were restricted by cyclic heat treatment. An important feature observed in the steel subjected to cyclic heat treatment was frequent crack deflection and crack tip blunting, which occurred at block and prior austenite grain boundaries (triple junctions). Therefore, grain refinement increased the probability of crack deflection and crack tip blunting. In addition, the relatively low dislocation density in cyclically heat-treated steel is believed to contribute to the suppression of plasticity-related damage nucleation, which is critically important for quasi-cleavage cracking.

1. Introduction

Hydrogen atoms, as the lightest and smallest atoms, can easily enter and diffuse into metallic materials either during manufacturing or by serving in an aggressive environment (e.g., high-pressure hydrogen gas and corrosive environment) [1], which induces a variety of degradation modes in materials by threatening their safety, durability, and performance. This phenomenon, known as hydrogen embrittlement (HE) [2], is rather obvious in high-strength steels (strength above ~650 MPa) since they are prone to hydrogen-related cracking [3,4]. Specifically, tempered martensitic steels currently play a crucial role in the automobile industry due to their high tensile strength (over 1 GPa) and excellent cost performance. Furthermore, they are regarded as prospective candidates for constructing a hydrogen-energy-based society by structuring related equipment, including pressure vessels, pipelines, and even tanks. However, the tensile strength of tempered martensitic steels significantly decreases in the presence of even a slight amount of hydrogen (0.26–0.29 mass ppm) [5]. Therefore, improving the HE resistance of tempered martensitic steels is required for practical and broad use in the current industry.

The primary role of dissolved hydrogen atoms is to interact with various lattice defects, such as vacancies, dislocations, and interfaces, which can accelerate microcrack nucleation/initiation and growth [4]. Once the crack starts to grow, the high stress triaxiality ahead of the crack tip can attract additional hydrogen to accumulate in its vicinity [6], which promotes further crack growth and associated catastrophic failure. Therefore, we must develop a microstructure design strategy for HE resistance in terms of (1) interactions between hydrogen and lattice defect evolution, (2) local hydrogen diffusivity at the crack tip, and (3) hydrogen-assisted microcrack growth. From the viewpoint of hydrogen-assisted crack growth, there are representative hydrogen-induced fracture modes in tempered martensitic steels: intergranular (IG) fracture [7] and quasi-cleavage (QC) fracture [8]. The hierarchical microstructure of lath martensite (including prior austenite grains (PAGs), martensite packets, blocks, and laths [9,10]) plays a crucial role in restricting hydrogen-assisted crack growth paths due to the presence of numerous martensite boundaries serving as obstacles at different spatial scales (i.e., prior austenite grain boundaries (PAGBs) at the dozens of microns scale and block (even lath) boundaries at the submicron scale [8]). Particularly when there is significant plastic

---

[*] Corresponding author.
E-mail address: motomichi.koyama.c5@tohoku.ac.jp (M. Koyama).

https://doi.org/10.1016/j.ijhydene.2024.05.327
Received 30 January 2024; Received in revised form 6 May 2024; Accepted 21 May 2024

deformation at the crack tip, the degree of crack blunting and the probability of cracking occurring near or on specific martensite boundaries act as factors controlling the resistance to hydrogen-assisted crack growth. In the case of QC crack growth, crack blunting occurs when the tip reaches the block boundaries and PAGBs. Crack blunting for the IG crack occurs when its tip meets portions of low-angle and Σ3 grain boundaries on PAGBs [11]. Therefore, increasing the number density of the boundaries is feasible for improving the HE resistance.

In general, refining the grain size of polycrystalline metallic materials can improve their mechanical properties [12,13] and increase the area of grain boundaries simultaneously, which can also improve the resistance to hydrogen-related IG fracture [14–16]. Fuchigami et al. examined the effect of PAG size on the HE susceptibility of tempered martensitic steel [17]. These authors suggested that refinement of the PAG reduces HE susceptibility by suppressing the formation of vacancies caused by interactions between dislocations since a decrease in PAG size reduces the slip length of dislocations and the density of geometrically necessary dislocations. Zhang et al. also investigated the HE phenomenon in tempered martensitic steel specimens with different grain sizes produced by cold deformation and subsequent heat treatment [18]. They tested three different cold deformation amounts (0%, 40%, and 80%, corresponding to average PAG sizes of 9.8, 6.1, and 4.3 μm, respectively) and revealed that PAG refinement improved the HE resistance.

Considering the abovementioned findings, there are two important challenges in furthering the understanding of the effect of PAG refinement and overcoming practical problems. The first challenge is to clarify the effect of PAG on hydrogen-related crack growth because crack blunting at a specific martensite boundary is a factor controlling resistance to HE. From this perspective, the crack morphology and local plasticity evolution associated with crack blunting are keys. In practice, cold deformation of tempered martensitic steels is challenging because the yield strength and flow stress are extremely high compared to those of other industrial metallic materials. Thus, the cold deformation process is not cost-effective [13] and cannot be used to produce relatively thick plates. Instead, for tempered martensitic steels, thermal cycling [19], which results in the repetition of austenite reversion and martensitic transformation, also results in significant PAG refinement [13,19–21], even for PAG sizes smaller than 5 μm. The hydrogen-related fracture behavior of grain-refined martensitic steels produced by cyclic thermal treatment has never been investigated.

Hence, in this study, we aim to clarify the following two aspects. First, we examined whether PAG refinement by cyclic thermal treatment had an advantage in terms of HE resistance similar to that in previous work. Second, the microstructural growth path and morphology of the cracks were investigated to determine the underlying effect of PAG size on the HE resistance of tempered martensitic steel.

2. Experiments

2.1. Material preparation

Seven-millimeter-thick steel plates with a chemical composition of 0.41C-0.2Si-0.61Mn-0.014P-0.003S-0.1Cu-0.06Ni-1.02Cr-0.17Mo (mass%) were prepared. Fig. 1 shows two heat treatment routes used to obtain tempered martensite with different PAG sizes, which have been confirmed in a recent publication [22]. A steel plate was austenitized at 900 °C for 1 h, followed by oil quenching; then, the plate was tempered at 600 °C for 1 h and oil quenched, as shown in Fig. 1(a). The steel heat-treated with a single cycle is referred to as the SC specimen. The other one underwent five cycles of rapid full austenitizing and quenching, as shown in Fig. 1(b). The steel heat-treated for multiple cycles is referred to as the MC specimen. Fig. 1(c) schematically shows the microstructural change during a thermal cycle. A lath martensite microstructure can be obtained after oil quenching. Because martensite contains numerous dislocations, subsequent austenitization results in the formation of new austenite at various high-angle boundaries in lath martensite. When quenched before significant grain growth occurs (e.g., within 5 min), the steel shows a fine lath martensite microstructure [23]. With decreasing austenite grain size, austenite tends to nucleate only at PAGBs. Therefore, the grain size saturates by achieving a balance between refinement by nucleation and grain growth after the completion of austenitization [13,19].

2.2. Mechanical tests, hydrogen charging, and microstructural characterization

The as-received materials were lathe-machined to fabricate sheet specimens (Fig. 3(a)) with gauge dimensions of 10 mm in length, 4 mm in width, and 1 mm in thickness. After machining, the tensile specimens were mechanically polished using emery papers #1000 and #2000 to remove scratches. Electrochemical hydrogen charging under different

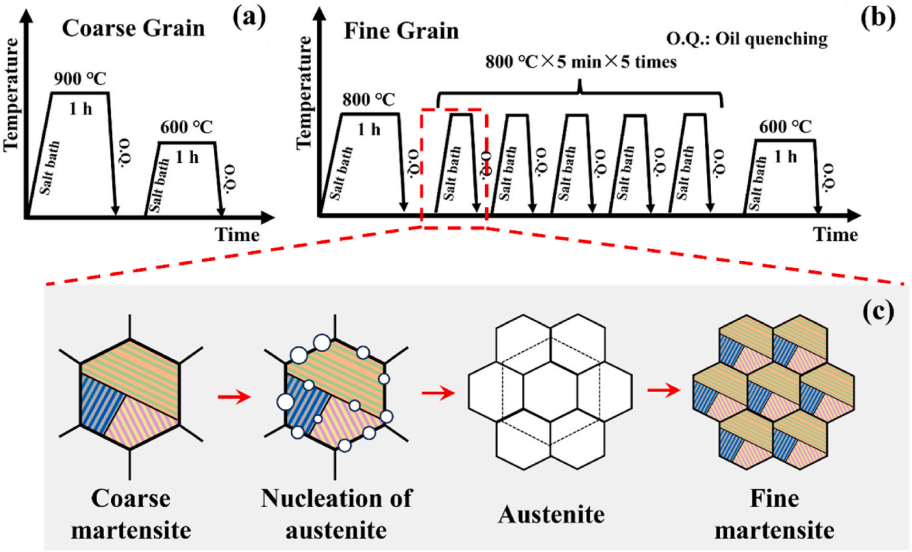

Fig. 1. Schematic illustrations of (a) heat treatment procedures for materials containing coarse PAGs and (b) PAG refinement by thermal cycling. (c) Schematic of PAG refinement by thermal cycling.

conditions was conducted before tensile tests, as listed in Table 1. The addition of NH_4SCN promotes hydrogen ingress into the specimen [24]. Hydrogen pre-charging was performed at ambient temperature for 96 h. After hydrogen pre-charging, the specimens were subjected to tensile testing at ambient temperature with an initial strain rate of 1×10^{-4}/s (corresponding to a cross-head displacement rate of 0.06 mm/min). The hydrogen content was measured after tensile testing using thermal desorption spectroscopy (TDS) at a heating rate of 200 °C/h. To avoid hydrogen release, the fractured specimens were preserved in liquid nitrogen until TDS was carried out. The cumulative hydrogen desorbed from ambient temperature to 300 °C was regarded as the diffusible hydrogen content because the hydrogen content in this regime corresponds to weaker binding states and diffusible states at room temperature. The diffusible hydrogen content is directly associated with HE-induced degradation [25,26].

After tensile testing, the variations in the mechanical properties of the SC and MC specimens under different hydrogen contents were summarized and compared to examine the enhancement in the HE resistance after grain refinement. Then, fractographic analysis was carried out through secondary electron imaging (SEI) at an accelerating voltage of 15 kV. The microstructural information surrounding the hydrogen-assisted cracks was extracted from the samples obtained from the interruption tests. The SC and MC specimens were hydrogen-charged in 3% NaCl aqueous solution with 3 g/L NH_4SCN and 10 A/m^2 (i.e., Condition C in Table 1), respectively. The hydrogen-charged specimens were subjected to tensile deformation until reaching the UTS and subsequently unloaded before fracture. The cracking behaviors of both tested steels were examined through SEI, electron channeling contrast imaging (ECCI), and electron backscatter diffraction (EBSD) measurements. The ECCI was operated at 30 kV, and EBSD measurements were conducted at 20 kV with a beam step size ranging from 50 to 100 nm. The martensite boundary classification was conducted using TSL-OIM and ARPGE software [27,28].

3. Results

3.1. Microstructures and mechanical tests

Fig. 2(a$_1$) and (b$_1$) show reference direction (RD/tensile axis)-inverse pole figure (IPF) maps of the SC and MC specimens before testing, and the microstructures in both cases consisted of lath martensite. Most PAGBs were identified if the boundaries included segments with misorientation angles within the range of 15–45° [9,29], as highlighted by the white dashed lines. Thermal cycling effectively refined the PAGs such that the average PAG sizes of the SC and MC specimens were approximately 30 and 5 μm, respectively, automatically measured as the average line intercept length. Along with the reduction in the average PAG size, the average size of the martensite blocks, which controls strength [30], also decreased, as summarized in Fig. 2(c). For the boundary length variation after thermal cycling shown in Fig. 2(d), the boundary length of PAGBs per area increased from 0.5 (SC) to 1.1 (MC) μm^{-1}, as calculated for identical observation areas. It is worth noting that the length per area of the block boundaries did not increase as much as the PAGBs after grain refinement (Fig. 2(d)). Fig. 2(a$_2$) and (b$_2$) show the corresponding kernel average misorientation (KAM) maps of the SC and MC specimens, respectively. Since the KAM values correspond to the geometrically necessary dislocation density [31–33], the higher KAM values in the SC specimen (Fig. 2(a$_2$)) than in the MC specimen (Fig. 2(b$_2$)) indicate that grain refinement decreases the initial dislocation density, probably due to a smaller requirement of slip for lattice invariant shear during martensitic transformation. Besides, the grain boundary area of the MC specimen increased with decreasing the mean grain size (Fig. 2(d)), thereby facilitating dislocation annihilation or rearrangement since the grain boundaries can serve as sink sources for dislocations during the grain refinement process [34].

Using the specimens shown in Fig. 3(a), the nominal stress−strain curves of the SC and MC specimens with and without hydrogen charging were obtained (Fig. 3). An obvious feature of the MC specimen under all the conditions was yielding. Specifically, the SC specimen always exhibited continuous yielding, whereas the apparent yield-drop phenomenon happened in all the MC specimens. The yield-drop phenomenon universally occurs in carbon steels and fine-grained metals and alloys [35]. The yield-drop is generally caused by the dislocation-locking mechanism by interstitial atoms, such as carbon, or carbides [36,37] and a lack of mobile dislocations [12]. According to the KAM maps in Fig. 2, the initial geometrically necessary dislocation density in the MC specimen was significantly lower than that in the SC specimen. Assuming that mobile dislocation density monotonically changes with geometrically necessary dislocation density [20], it would imply a less chance of activation of dislocation motion and dislocation interactions for creating dislocation sources that can multiply dislocations [12]. Furthermore, the dislocation locking effect of solute carbon and fine cementite precipitates becomes significant particularly after tempering [37], which assists in the occurrence of a yield drop.

The SC and MC specimens exhibited almost identical mechanical properties when no hydrogen was introduced into them electrochemically (Fig. 3(a)), whereas the improvement in the HE resistance through grain refinement became significant with increasing hydrogen content (Fig. 3(b–d)). The diffusible hydrogen contents in the SC and MC specimens pre-charged under conditions A, B, and C were detected via TDS measurements. Only one peak was observed in all TDS profiles of hydrogen-charged specimens (Fig. 4(a–c)). It is worth noting that the elongation of the MC specimen did not deteriorate due to hydrogen uptake until a hydrogen content of approximately 2.0 mass ppm was reached, and the gap between the elongations of the SC and MC specimens increased with increasing hydrogen content (Fig. 4(d)).

3.2. Fractographic analysis and crack morphologies in SC specimens

Fig. 5 shows a summary of the fracture surfaces of the SC and MC specimens obtained from different testing conditions (with and without hydrogen charging). When no hydrogen was introduced into the specimens, both steels exhibited a typical ductile fracture feature involving dimples in the center of the fracture surfaces and obvious necking, as highlighted by the yellow dashed lines in Fig. 5(a$_1$) and (a$_2$). For both the hydrogen-charged SC and MC specimens, fracture occurred prematurely with increasing hydrogen content before substantial progress of necking, i.e., Conditions A to C, based on the comparison from Fig. 5(a)–(d). The fracture mode also changed, especially under Condition C (i.e., 3% NaCl + 3 g/L NH_4SCN + 10 A/m^2), as shown in Fig. 5(d$_1$) and (d$_2$), which were examined in detail because they exhibited the most distinct HE phenomenon (Fig. 3(d)). In this section, we first note the characteristics of HE in the SC specimen.

Fig. 6(a) shows the region highlighted in Fig. 5(d$_1$), which shows the fracture surface of the SC specimen with a hydrogen content of 3.40 mass ppm (Fig. 4(c)), which exhibits the most significant degradation in mechanical properties, especially in elongation, which decreased from 14.7% to 3.6%. The mixed fracture modes containing IG and QC fracture features can be seen in Fig. 6(b$_1$), and one IG fracture surface was extracted and observed at high magnification (Fig. 6(b$_2$)); moreover, some tear ridges could be observed (highlighted by yellow arrows), reflecting the participation of plasticity in IG cracking. Fig. 6(c) is the magnified SE image of the other highlighted region in Fig. 5(d$_1$). The PAG geometries were still identifiable in Fig. 6(c$_1$) with the assistance of

Table 1
List of electrochemical hydrogen-charging conditions.

	Aqueous solution	Current density
Condition A	0.1 N NaOH +5 g/L NH_4SCN	100 A/m^2
Condition B	3% NaCl +3 g/L NH_4SCN	5 A/m^2
Condition C	3% NaCl +3 g/L NH_4SCN	10 A/m^2

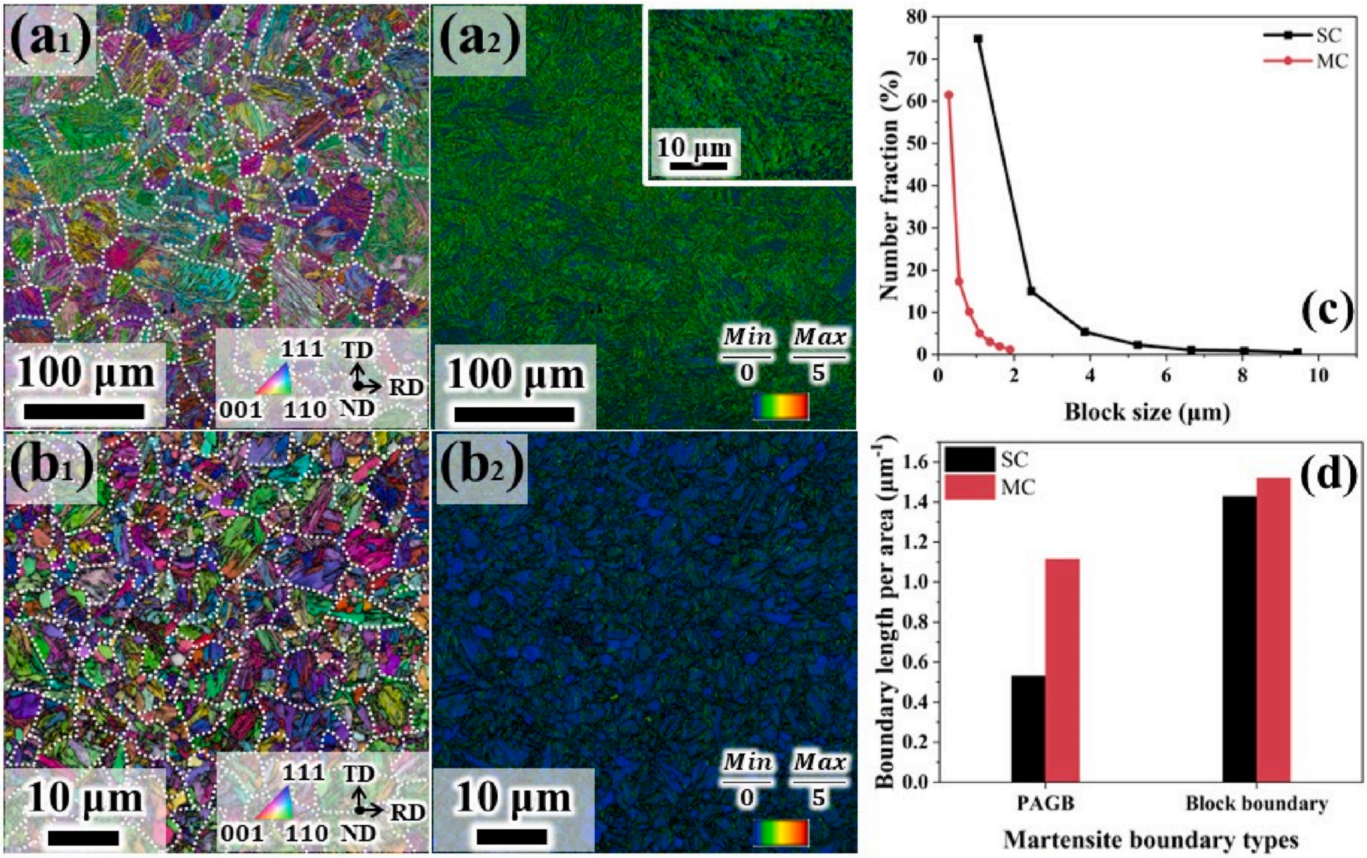

Fig. 2. (a_1) and (b_1) RD-IPF maps of the microstructures of the SC and MC specimens after heat treatments, respectively. (a_2) and (b_2) Corresponding KAM maps of (a_1) and (b_1). The beam step sizes for the measurements of (a) and (b) were 0.35 and 0.10 μm, respectively. Since KAM depends on step size, a KAM map taken at the same step size (0.10 μm) as (b_2) with a high magnification for the SC specimen is also shown as the inset of (a_2), which indicates the almost identical distribution of KAM. (c) Number fractions of block sizes automatically calculated from the TSL-OIM software in the form of intercept lengths. (d) Boundary length per area of the PAGBs and block boundaries in the SC and MC specimens.

white dashed line highlighting, and some secondary cracks appeared around the PAG contours and propagated along the normal direction of the figure, as highlighted by yellow arrows. However, a significant part of the fracture surface was covered by dimples instead of a relatively smooth grain boundary surface (Fig. 6(c_2)).

Fig. 7(a) shows an overview of the SE image of the hydrogen-related crack in the SC specimen obtained from the interruption test. The image shows a tortuous crack morphology with an inhomogeneous crack opening degree. The inhomogeneous variation in the crack opening degree reflects the discontinuous crack growth associated with crack tip blunting. Fig. 7(b) shows a magnified image of the highlighted region of Fig. 7(a). The PAGBs are highlighted by white dashed lines. The solid white and red lines represent the crack paths along the PAGBs (IG cracks) and across the PAG (QC cracks), respectively. The mixed crack growth paths correspond to the mixed fractographic features (Fig. 6(b)). Similar phenomena also appeared in the crack tip region, as shown in Fig. 7(c) and (d). Unlike the crack growth behavior in Fig. 7(b), the cracking behavior around the crack tip (Fig. 7(c)) was discontinuous, including both crack arrest and crack regrowth through crack coalescence. In addition, some microvoids were observed along the IG crack path (i.e., PAGBs), highlighted by yellow arrows, according to the boundary classification in Fig. 7(d). As shown in Fig. 7(b) and (d), crack deflection resulting in a tortuous morphology occurred at the PAGBs for QC cracks and at PAGB triple junctions for IG cracks, as also reported in our previous paper [7].

3.3. Fractographic analysis and crack morphologies in MC specimens

Fig. 8 shows a magnified image of the fracture surface of the MC specimen with a hydrogen content of 3.35 mass ppm, which corresponds to the relatively flat region highlighted by the yellow rectangle in Fig. 5 (d_2). This region contains apparent ductile tearing, which indicates that plasticity contributes more to the fracture process in the MC specimen than in the SC specimen with a similar hydrogen content. Furthermore, the macroscopically flat region exhibited tortuous features with numerous tear ridges. Both tear ridges and river-like patterns appear on the further magnified fractograph (Fig. 8(b)), reflecting the typical QC fracture feature and indicating that the QC crack growth process dominated the premature failure and related reduction in the elongation of the hydrogen-charged MC specimen.

Fig. 9(a) shows a hydrogen-related crack in the MC specimen after the tensile test was interrupted. The PAGBs around the cracks were identified, as highlighted in the magnified RD-IPF map (Fig. 9(b)). Compared to that of the SC specimen, a more significant length fraction of crack paths within the PAG was observed in the MC specimen. Specifically, the major portion of the crack was along packet and block boundaries or crossed the martensite block/lath (Fig. 9(b)), as shown in Fig. 9(c), and the proportion of IG cracking (along PAGBs) was merely 10.3%. The statistical results obtained from EBSD measurements corresponded to the QC fractographic features shown in Fig. 8.

Fig. 10(a) and (b) exhibit the local plasticity evolution involved in the crack growth in both the SC and MC specimens. The observation regions correspond to those shown in Figs. 7(d) and Fig. 9(b). Since plasticity evolution leaves dislocation-related orientation distortion, the

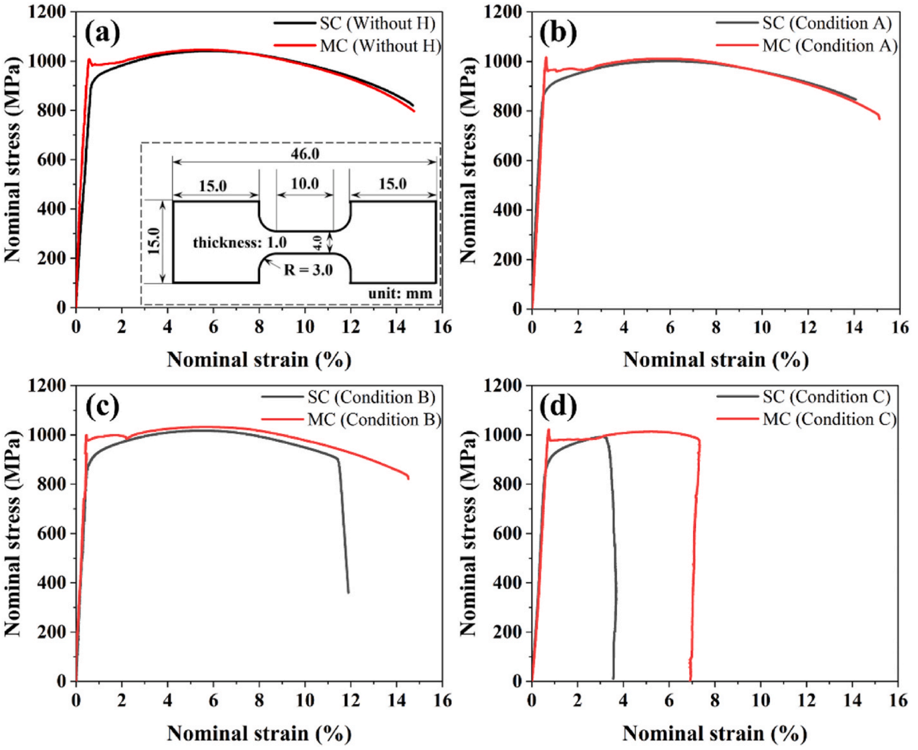

Fig. 3. Nominal stress-strain curves of the SC and MC specimens tested (a) without hydrogen pre-charging and (b–d) with hydrogen pre-charging under Conditions A, B, and C in Table 1, respectively. The inset in (a) shows the specimen dimensions for tensile testing (unit: mm).

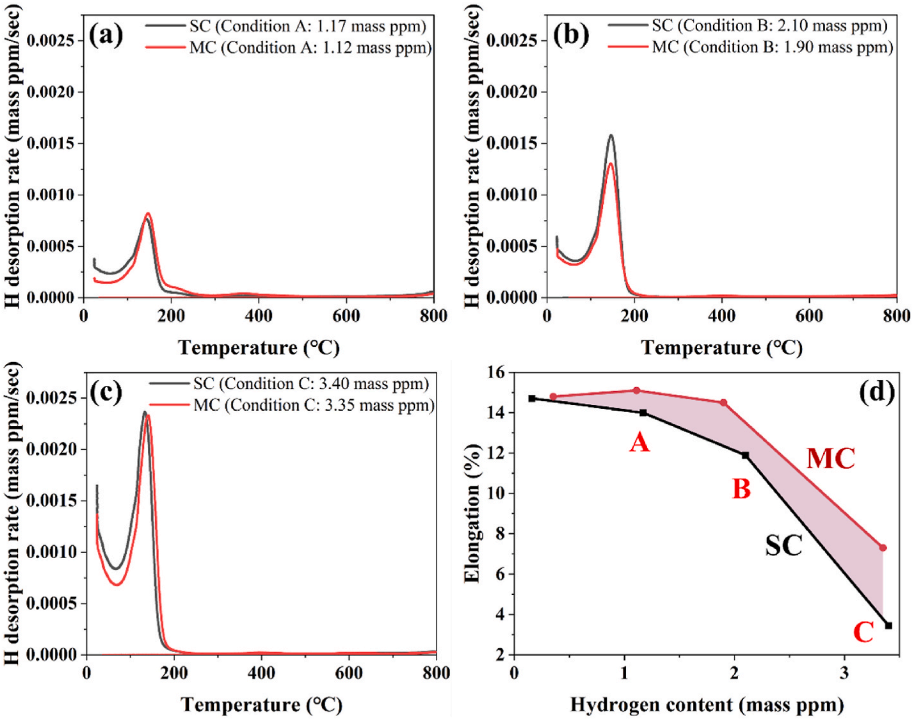

Fig. 4. (a–c) TDS profiles of the SC and MC specimens pre-charged under three different Conditions A, B, and C in Table 1, respectively. (d) Elongations plotted against the hydrogen content. The points A, B, and C in (d) represent the hydrogen pre-charging Conditions A, B, and C in Table 1.

significance of plasticity during crack growth can be evaluated by orientation mapping. The orientation distortion can be quantified by measurements of grain reference orientation deviation (GROD), which is defined as the difference between an orientation at an arbitrary point and the corresponding average orientation of the grain [38,39]. Furthermore, the grain-averaged GROD has been shown to be linearly related to plastic strain even near a notch or crack tip, i.e., grain orientation spread (GOS) [11,29]. Fig. 10(a) and (b) show the GOS maps around the hydrogen-related cracks in the SC and MC specimens. The distributions of the GOS values beneath the crack path in both cases

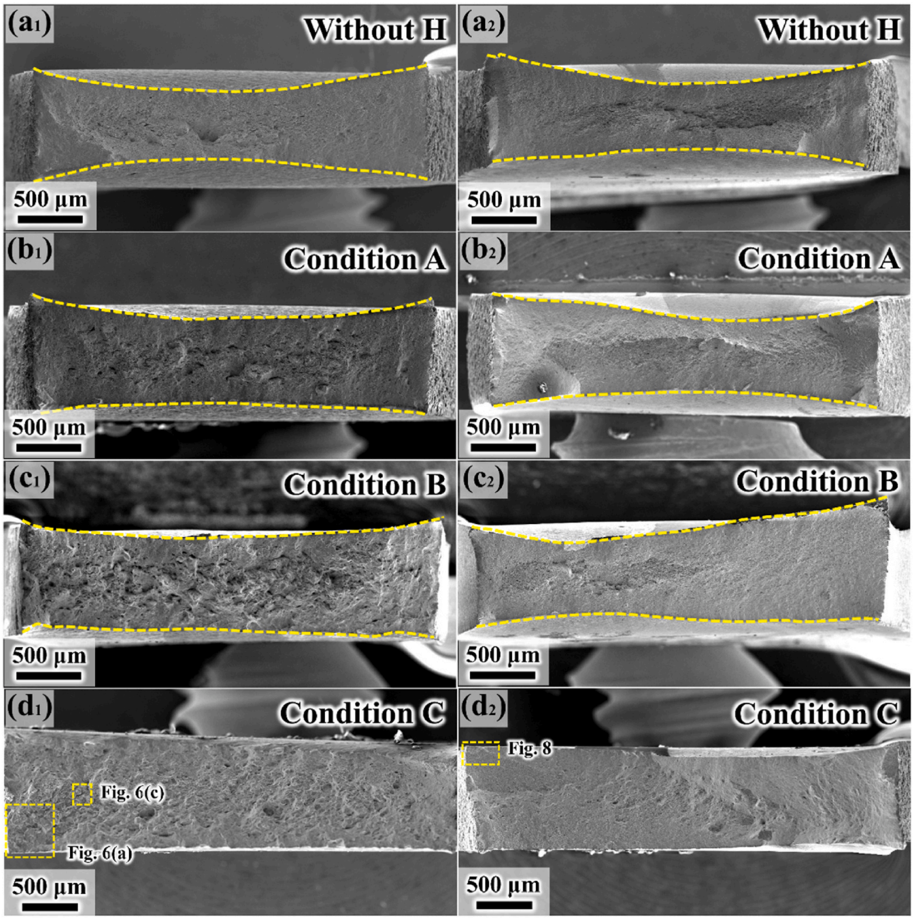

Fig. 5. Fracture surfaces of the noncharged (a_1) SC and (a_2) MC specimens, hydrogen-charged (b_1) SC and (b_2) MC specimens in Condition A, hydrogen-charged (c_1) SC and (c_2) MC specimens in Condition B, and hydrogen-charged (d_1) SC and (d_2) MC specimens in Condition C.

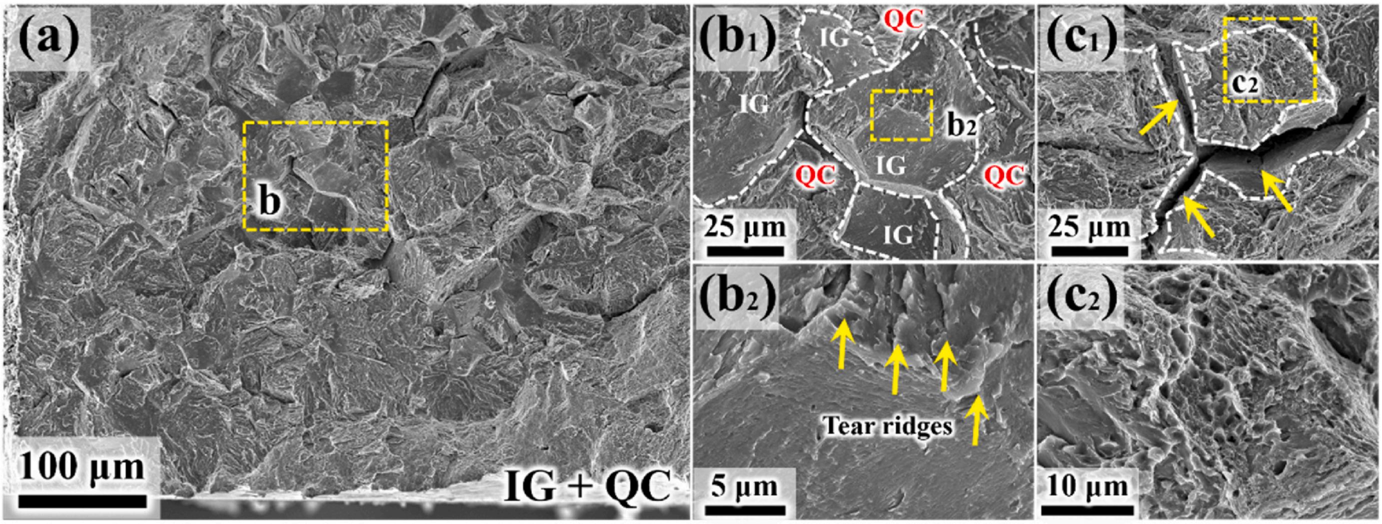

Fig. 6. (a) Fracture surface reflecting mixed features containing IG and QC fractures in the region highlighted in Fig. 5(d_1). (b) and (c) Magnified images showing the IG fracture and the morphological features of the IG fracture surfaces. The white dashed lines in (b) and (c) highlight the grain geometric contours.

were statistically analyzed, as shown in Fig. 10(c). The GOS values around the hydrogen-assisted cracks in the SC specimen were greater than those in the MC specimen. Specifically, approximately 80% of the GOS values in the MC specimen were lower than 3 deg. In contrast, the distribution of GOS values in the SC specimen was more gradual than that in MC specimen, and almost 40% of the GOS values were above 4 deg.

The crack tip region highlighted in Fig. 9(b) was further characterized via ECC imaging, as exhibited in Fig. 11(a). The crack morphology was tortuous due to the crack deflection during the growth process. A

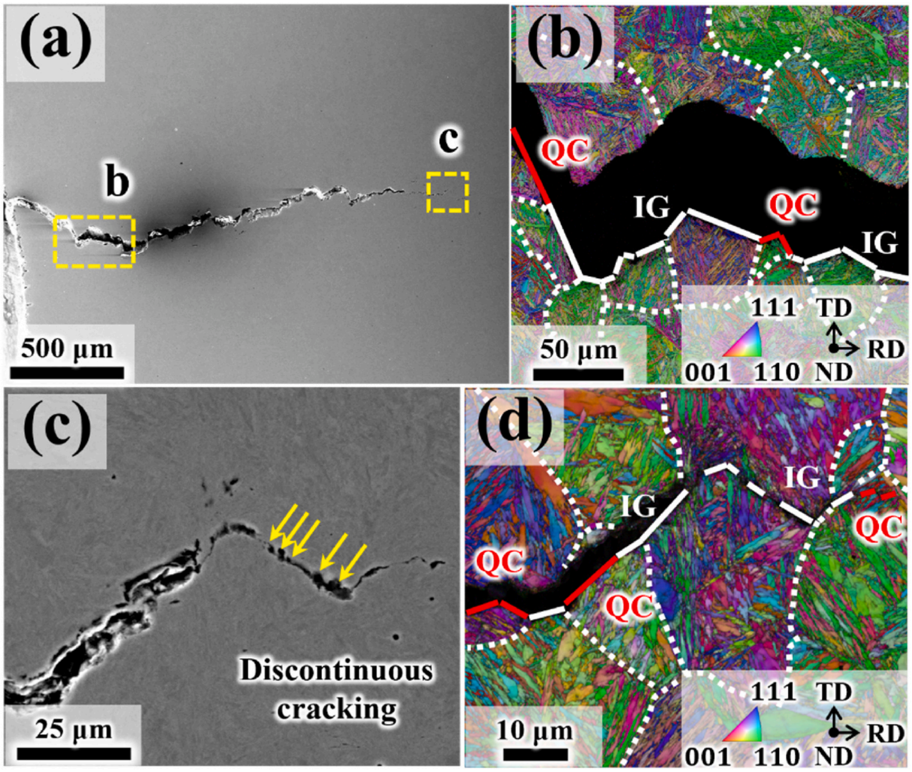

Fig. 7. (a) Overview of the hydrogen-related crack morphology in the SC specimen obtained from the interruption test. (b) RD-IPF map reflecting the microstructural information around the crack coalescence region highlighted in (a). (c) A magnified SE image of the crack tip. (d) RD-IPF map corresponding to the region in (c).

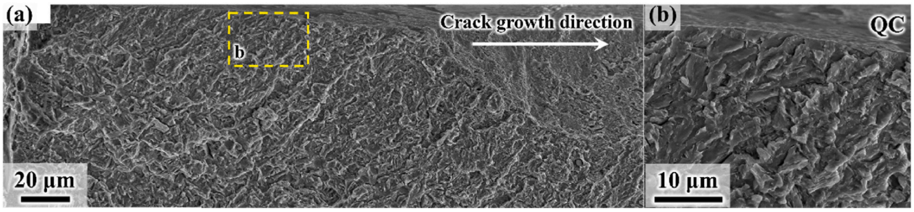

Fig. 8. (a) SE image of the region highlighted in Fig. 5(d$_2$) corresponding to the fracture surface of the MC specimen with a hydrogen content of 3.35 mass ppm. (b) Magnified SE image reflecting the QC fracture features.

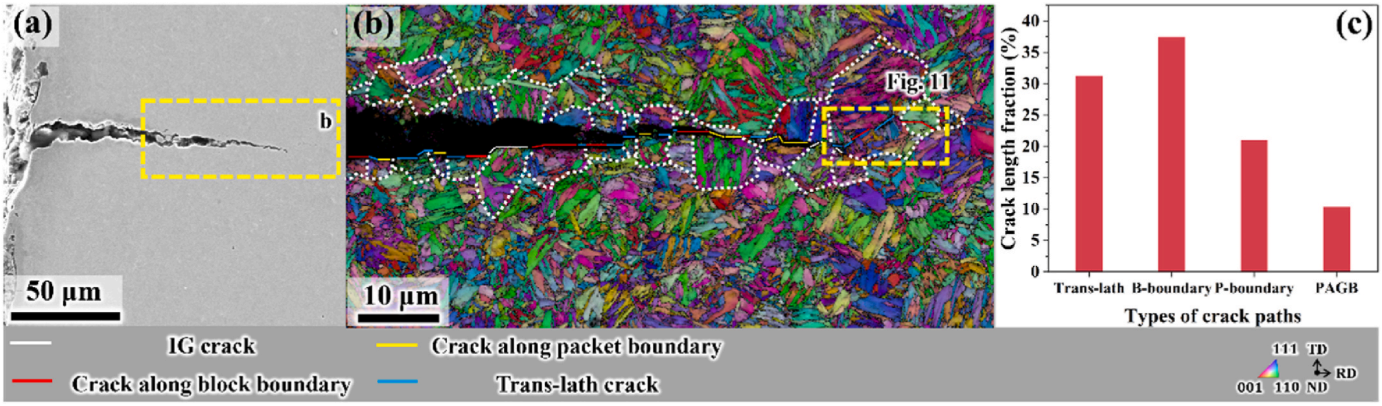

Fig. 9. (a) Overview of the hydrogen-related cracks in the MC specimen obtained from the interruption test. (b) RD-IPF map corresponding to the region highlighted in (a). (c) Relationships between hydrogen-assisted crack length fractions and crack path types. The abbreviations for the B-boundary and P-boundary represent the block boundary and packet boundary, respectively.

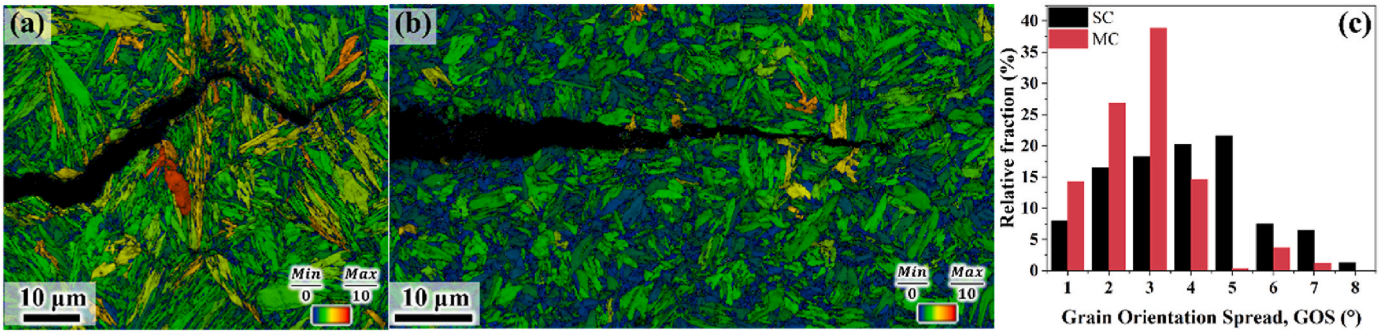

Fig. 10. GOS maps around the hydrogen-related cracks in the SC and MC specimens, which correspond to the regions in (a) Fig. 7(d) and (b) Fig. 9(b). (c) Statistical analysis of the GOS values along the crack paths in the SC and MC specimens.

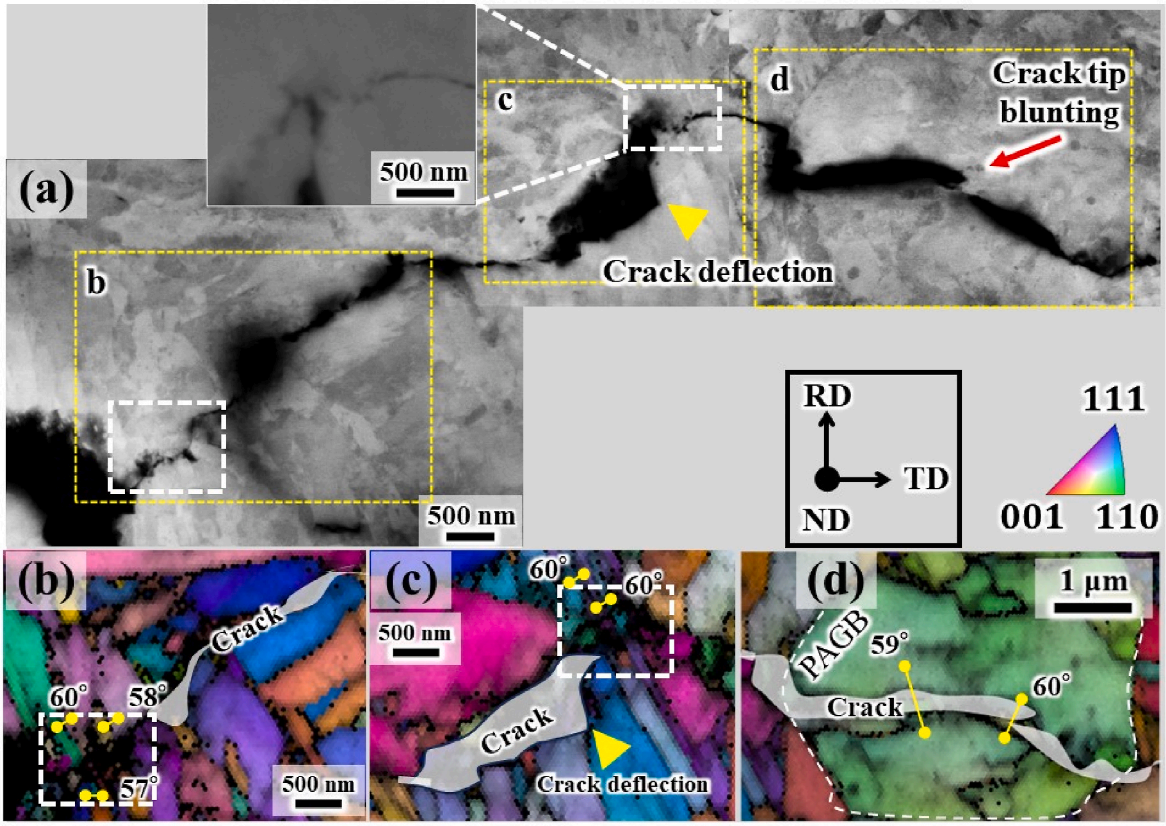

Fig. 11. (a) ECC images showing the crack morphology of the MC specimen. The inset shows a corresponding SE image. (b–d) RD-IPF maps of the regions highlighted in (a) where crack deflection and nanoscale crack tip blunting occurred.

typical crack deflection marked by yellow arrowheads was examined through EBSD measurements. Based on the RD-IPF map in Fig. 11(c), crack deflection occurred when the martensite block boundaries were met with a misorientation angle of approximately 60° [29]. In addition to the crack deflection, the interaction between the hydrogen-related crack and block boundaries could induce crack tip blunting, as highlighted by the white dashed rectangles in Fig. 11(a)–(c). The inset in Fig. 11(a) is an SE image, which shows the microcrack path [40]. Furthermore, there was a blunt crack tip marked by a red arrow in the ECC image (Fig. 11(a)). Based on the misorientation measurements, the crack path of these two blunted cracks was along the block boundary, and one of the blunt crack tips was located at the PAGB (Fig. 11(d)).

4. Discussion

4.1. *Restriction of IG cracking by multicycle heat treatment: grain refinement effect*

A comparison of the mechanical properties obtained from the SC and MC specimens illustrated that grain refinement by thermal cycling did not obviously affect the UTS or elongation when hydrogen was not introduced (Fig. 3). Therefore, we can compare the HE resistance of the SC and MC specimens with an almost identical strength [22] (tensile strength is a crucial factor affecting the HE sensitivity of metallic materials [41,42]). When the hydrogen content was high (3.40 mass ppm), cracking on PAGBs played a key role in the premature failure of the SC specimen (Fig. 7(b)). The preferential selection of PAGBs as the primary crack path is due to hydrogen localization [43,44] and impurity segregation [45] at the boundaries. As a secondary path, crack growth within the PAG interior was also observed in the region containing the crack tip (Fig. 7(c) and (d)), implying that QC fracture also contributed to hydrogen-assisted crack growth in the SC specimen. In this section, we note the effect of cyclic heat treatment on the IG cracking behavior.

The participation of IG cracking in hydrogen-assisted crack growth was significantly suppressed in the MC specimen (Fig. 9(b)). A decrease in grain size increases the grain boundary area in a unit volume (Fig. 2(d)); thus, the amount of hydrogen per unit length of PAGBs decreases [14] when the hydrogen content is similar (e.g., 3.40 and 3.35 mass ppm in this study, as shown in Fig. 4(c)). Furthermore, stress concentrations can be reduced by grain refinement [15,22,46,47]. In addition, since the initial dislocation density was reduced via cyclic heat treatment (Fig. 2(a_2) and (b_2)), the amount of hydrogen transported by dislocations to the PAGBs would be limited at a finite time for tensile testing [48]. These factors suppressed the cracking along PAGBs due to hydrogen-induced decrease in the boundary cohesive energy [49,50] in the MC specimen when compared with that in the SC specimen with a similar average hydrogen content.

Another possible factor causing IG cracking is hydrogen-enhanced local plasticity (HELP) evolution [51–53]. It is also noteworthy that dislocation gliding on the slip plane parallel to the habit plane within the block [54,55] beneath the crack path can be prone to be activated by the presence of hydrogen. The enhanced dislocation motion, coupled with the hydrogen effect, is impinged at PAGBs, plausibly forming an embryo of nanovoids/cracks [7]. This type of nanovoid was observed along the PAGBs accompanying the discontinuous IG crack growth process of the SC specimen (Fig. 7(c) and (d)), which might correspond to plasticity traces or microdimples on the IG fracture surfaces (Fig. 6(b_2) and (c_2)). In addition, according to the overview of the fracture surface in Fig. 5(d_1), the failure process of the SC specimen occurred from left to right; thus, the change in the features of the IG fracture surfaces from tear ridges (Fig. 6(b_2)) to microdimples accompanying severe secondary cracking (Fig. 6(c_2)) happened in the course of hydrogen-assisted crack growth, indicating the plasticity evolution became crucial in IG cracking. The relatively high dislocation density in the block/lath (Fig. 2(a_2)) implies that this plasticity participated in the IG cracking trend since sufficient mobile dislocations ensured the deformation ability of the matrix. Consequently, compared with that of the SC specimen, the GOS of the MC specimen was relatively lower near the crack path (Fig. 10(c)), even though the elongation of the SC specimen tested under Condition C was merely half of that of the MC specimen (Fig. 3(d)). Ultimately, the HELP-related formations of nanovoids/cracks at PAGBs were also restricted by the cyclic heat treatment.

After hydrogen-related crack nucleation, the crack grew until failure. In this context, crack deflection and crack tip blunting are important factors controlling failure resistance. In general, martensitic steels exhibit crack deflection and crack tip blunting at block boundaries and PAGB triple junctions [7]. These deflection and blunting behaviors frequently appeared in Fig. 11. Therefore, grain refinement increased the probability of crack tip blunting, which is regarded as an important factor for increasing the crack growth resistance. Hence, both the formation and growth of IG cracking could be limited in the MC specimen.

4.2. Restriction on QC cracking: crack blunting behavior

In tempered martensitic steels, the IG and QC cracking modes are competitive and depend on the hydrogen content, material's strength, and microstructure size. Because the SC specimen exhibited both IG and QC fractures, QC cracking and IG cracking must be suppressed to obtain significantly improved macroscopic mechanical properties. In this context, the lower initial dislocation density in the MC specimen than in the SC specimen directly affects the deformation ability of the matrix and the resistance to QC cracking because QC crack nucleation in steels occurs as a result of dislocation-dislocation interactions [56–59].

Furthermore, the grain refinement in the MC specimen also plays a key role in QC crack growth because crack tip blunting, which controls the crack growth resistance, occurs when the QC crack reaches block and PAG boundaries [8,57]. Specifically, PAGBs play a critical role in microcrack arrest and crack tip blunting when IG crack growth is completely suppressed [8]. The block boundaries were also observed to act as secondary sites for crack tip blunting in the MC specimen, which induced apparent crack deflection when QC crack growth was impeded by a block boundary, as highlighted by the yellow arrowhead in the ECC image (Fig. 11(a)) and RD-IPF map (Fig. 11(c)). Hence, grain refinement in the MC specimen increased the probability of crack tip blunting at martensite boundaries, which prevented QC crack growth.

According to our previous study [8], further growth of QC cracks after their arrest requires the formation of nanovoids ahead of the crack tip and their subsequent coalescencewith the main crack. In this regard, the fine sizes of the blocks and PAG in the MC specimen restrict the plasticity evolution around the crack path (Fig. 10(c)). Thus, the grain refinement effect coupled with the lower initial dislocation density in the MC specimen would have also contributed to not only arresting the QC crack but also reducing the probability of nanovoid formation required for further growth.

5. Conclusions

In this study, the effects of cyclic heat treatment on hydrogen-assisted cracking in a tempered martensitic steel were investigated in terms of microstructural crack paths and morphologies. The cyclic heat treatment decreased the grain size and initial dislocation density, which improved the HE resistance. Specifically, the cyclic heat treatment restricted both the hydrogen-assisted IG and QC crack growth. The details of the conclusions are as follows.

(1) The cyclic heat treatment did not obviously affect the mechanical properties when hydrogen was not introduced into the specimens, although the grain size distinctly decreased. With increasing hydrogen content, a significant difference in elongation between the specimens with and without cyclic heat treatment occurred. For instance, with a diffusible hydrogen concentration of approximately 3.4 mass ppm (specifically, 3.35 and 3.40 mass ppm), cyclic heat treatment suppressed both the IG and QC fractures owing to grain refinement and a reduction in initial dislocation density.

(2) The primary role of cyclic heat treatment in improving IG cracking resistance is grain refinement. Grain refinement reduces the amount of hydrogen trapped per unit length of PAGBs at similar hydrogen content levels, which suppresses IG crack initiation. IG crack growth was impeded by the reduced crack length along PAGBs and the increased number of grain boundary triple junctions in the fine-grain specimen. In addition, the plasticity evolution around the crack path was low in the cyclically heat-treated specimen, which also contributed to suppressing crack nucleation associated with dislocation–PAGB interactions.

(3) For QC crack initiation and growth, the low initial dislocation density in the cyclically heat-treated specimen directly affects the critical amount of deformation for QC crack nucleation. Furthermore, owing to grain refinement, the high densities of block boundaries and PAGBs increase the probabilities of crack tip blunting and crack path deflection. Furthermore, the plasticity evolution around the crack path is restricted in the cyclically heat-treated specimen, which can also reduce the probability of nanovoid nucleation associated with QC crack growth.

CRediT authorship contribution statement

Tingshu Chen: Data curation, Formal analysis, Investigation, Writing – original draft. **Yuhei Ogawa:** Conceptualization, Investigation, Writing – review & editing. **Motomichi Koyama:**

Conceptualization, Investigation, Supervision, Validation, Writing – review & editing.

Declaration of competing interest

The authors declare that they have no known competing financial interests or personal relationships that could have appeared to influence the work reported in this paper.

References

[1] Gangloff RP, Somerday BP. Gaseous hydrogen embrittlement of materials in energy technologies, vol. 2. Cambridge (UK): Woodhead Publishing Limited; 2012. https://doi.org/10.1533/9780857095374.

[2] Nagumo M. Fundamentals of hydrogen embrittlement. first ed. Tokyo JPN: Springer; 2016. https://doi.org/10.1007/978-981-10-0161-1.

[3] Akiyama E, Matsukado K, Wang M, Tsuzaki K. Evaluation of hydrogen entry into high strength steel under atmospheric corrosion. Corrosion Sci 2010;52:2758–65. https://doi.org/10.1016/j.corsci.2009.11.046.

[4] Sun B, Lu W, Gault B, Ding R, Makineni SK, Wan D, et al. Chemical heterogeneity enhances hydrogen resistance in high-strength steels. Nat Mater 2021;20:1629–34. https://doi.org/10.1038/s41563-021-01050-y.

[5] Nagao A, Hayashi K, Oi K, Mitao S. Effect of uniform distribution of fine cementite on hydrogen embrittlement of low carbon martensitic steel plates. ISIJ Int 2012;52:213–21. https://doi.org/10.2355/isijinternational.52.213.

[6] Takeda Y, McMahon CJ. Strain controlled vs stress controlled hydrogen induced fracture in a quenched and tempered steel. Metall Trans A, Phys Metall Mater Sci 1981;12(A):1255–66. https://doi.org/10.1007/BF02642339.

[7] Chen T, Chiba T, Koyama M, Akiyama E, Takai K. Factors distinguishing hydrogen-assisted intergranular and intergranular-like fractures in a tempered lath martensitic steel. Metall Mater Trans A Phys Metall Mater Sci 2022;53:1645–58. https://doi.org/10.1007/s11661-022-06608-2.

[8] Chen T, Chiba T, Koyama M, Shibata A, Akiyama E, Takai K. Hierarchical characteristics of hydrogen-assisted crack growth and microstructural strain evolution in tempered martensitic steels: case of quasi-cleavage fracture. Metall Mater Trans A Phys Metall Mater Sci 2021;52:4703–13. https://doi.org/10.1007/s11661-021-06423-1.

[9] Morito S, Tanaka H, Konishi R, Furuhara T, Maki T. The morphology and crystallography of lath martensite in Fe-C alloys. Acta Mater 2003;51:1789–99. https://doi.org/10.1016/S1359-6454(02)00577-3.

[10] Kitahara H, Ueji R, Tsuji N, Minamino Y. Crystallographic features of lath martensite in low-carbon steel. Acta Mater 2006;54:1279–88. https://doi.org/10.1016/j.actamat.2005.11.001.

[11] Chen T, Koyama M, Chiba T, Akiyama E, Takai K. Mesoscale quantification of grain boundary character and local plasticity in hydrogen-assisted intergranular and intergranular-like cracking paths in tempered martensitic steel. Mater Sci Eng, A 2023;886:145718. https://doi.org/10.1016/j.msea.2023.145718.

[12] Tanaka I, Tsuji N, Inui H. The plaston concept. Singapore: Springer; 2022. https://doi.org/10.1007/978-981-16-7715-1.

[13] Furuhara T, Kikumoto K, Saito H, Sekine T, Ogawa T, Morito S, et al. Phase transformation from fine-grained austenite. ISIJ Int 2008;48:1038–45. https://doi.org/10.2355/isijinternational.48.1038.

[14] Park C, Kang N, Liu S. Effect of grain size on the resistance to hydrogen embrittlement of API 2W Grade 60 steels using in situ slow-strain-rate testing. Corrosion Sci 2017;128:33–41. https://doi.org/10.1016/j.corsci.2017.08.032.

[15] Koyama M, Ichii K, Tsuzaki K. Grain refinement effect on hydrogen embrittlement resistance of an equiatomic CoCrFeMnNi high-entropy alloy. Int J Hydrogen Energy 2019;44:17163–7. https://doi.org/10.1016/j.ijhydene.2019.04.280.

[16] Cho L, Bradley PE, Lauria DS, Connolly MJ, Seo EJ, Findley KO, et al. Effects of hydrogen pressure and prior austenite grain size on the hydrogen embrittlement characteristics of a press-hardened martensitic steel. Int J Hydrogen Energy 2021;46:24425–39. https://doi.org/10.1016/j.ijhydene.2021.05.005.

[17] Fuchigami H, Minami H, Nagumo M. Effect of grain size on the susceptibility of martensitic steel to hydrogen-related failure. Phil Mag Lett 2006;86:21–9. https://doi.org/10.1080/09500830500482316.

[18] Zhang D, Li W, Gao X, Fu L, Guo J, Zhang J, et al. Effect of cold deformation before heat treatment on the hydrogen embrittlement sensitivity of high-strength steel for marine risers. Mater Sci Eng, A 2022;845:143220. https://doi.org/10.1016/j.msea.2022.143220.

[19] Grange RA. The rapid heat treatment of steel. Metall Trans A 1971;2:65–78. https://doi.org/10.1007/BF02662639.

[20] Hidalgo J, Santofimia MJ. Effect of prior austenite grain size refinement by thermal cycling on the microstructural features of as-quenched lath martensite. Metall Mater Trans A Phys Metall Mater Sci 2016;47:5288–301. https://doi.org/10.1007/s11661-016-3525-4.

[21] Nasiri Z, Ghaemifar S, Naghizadeh M, Mirzadeh H. Thermal mechanisms of grain refinement in steels: a review. Met Mater Int 2021;27:2078–94. https://doi.org/10.1007/s12540-020-00700-1.

[22] Ogawa Y, Kuriyama K, Koyama M. Dual grain size-effects on hydrogen-assisted fatigue crack growth in 1 GPa-class medium-carbon martensitic steel. Int J Hydrogen Energy 2023;50:108–15. https://doi.org/10.1016/j.ijhydene.2023.08.317.

[23] Park M., Shibata A., Tsuji N. Challenging ultra grain Refinement of ferrite in low-C steel only by heat treatment, Front Mater. vol. 7; 2020. p. 1–10. 604792 doi: 10.3389/fmats.2020.604792.

[24] Takagi S, Toji Y. Application of NH 4SCN aqueous solution to hydrogen embrittlement resistance evaluation of ultra-high strength steels. ISIJ Int 2012;52:329–31. https://doi.org/10.2355/isijinternational.52.329.

[25] Takai K, Watanuki R. Hydrogen in trapping states innocuous to environmental degradation of high-strength steels. ISIJ Int 2003;43:520–6. https://doi.org/10.2355/isijinternational.43.520.

[26] Wang M, Akiyama E, Tsuzaki K. Effect of hydrogen on the fracture behavior of high strength steel during slow strain rate test. Corrosion Sci 2007;49:4081–97. https://doi.org/10.1016/j.corsci.2007.03.038.

[27] Cayron C. ARPGE: a computer program to automatically reconstruct the parent grains from electron backscatter diffraction data. J Appl Crystallogr 2007;40:1183–8. https://doi.org/10.1107/S0021889807048777.

[28] Suikkanen PP, Cayron C, DeArdo AJ, Karjalainen LP. Crystallographic analysis of martensite in 0.2C-2.0Mn-1.5Si-0.6Cr steel using EBSD. J Mater Sci Technol 2011;27:920–30. https://doi.org/10.1016/S1005-0302(11)60165-5.

[29] Chen T, Koyama M, Ogawa Y, Matsunaga H, Akiyama E. Martensite boundary characteristics on cycle- and time-dependent fatigue crack growth paths of tempered lath martensitic steels in a 90 MPa gaseous hydrogen atmosphere. Metall Mater Trans A Phys Metall Mater Sci 2023;54:2512–8. https://doi.org/10.1007/s11661-023-07041-9.

[30] Long S, Liang Y, Jiang Y, Liang Y, Yang M. Materials Science & Engineering A Effect of quenching temperature on martensite multi-level microstructures and properties of strength and toughness in. Mater Sci Eng, A 2016;676:38–47. https://doi.org/10.1016/j.msea.2016.08.065.

[31] Calcagnotto M, Ponge D, Demir E, Raabe D. Orientation gradients and geometrically necessary dislocations in ultrafine grained dual-phase steels studied by 2D and 3D EBSD. Mater Sci Eng, A 2010;527:2738–46. https://doi.org/10.1016/j.msea.2010.01.004.

[32] Wright SI, Nowell MM, Field DP. A review of strain analysis using electron backscatter diffraction. Microsc Microanal 2011;17:316–29. https://doi.org/10.1017/S1431927611000055.

[33] Rui SS, Han QN, Wang X, Li S, Ma X, Su Y, et al. Correlations between two EBSD-based metrics Kernel Average Misorientation and Image Quality on indicating dislocations of near-failure low alloy steels induced by tensile and cyclic deformations. Mater Today Commun 2021;27:102445. https://doi.org/10.1016/j.mtcomm.2021.102445.

[34] Humphreys FJ, Matherly M. Recrystallization and related annealing phenomena. Pergamon; 2004. https://doi.org/10.1016/B978-0-08-044164-1.X5000-2.

[35] Gao S, Chen M, Joshi M, Shibata A, Tsuji N. Yielding behavior and its effect on uniform elongation in if steel with various grain sizes. J Mater Sci 2014;49:6536–42. https://doi.org/10.1007/s10853-014-8233-0.

[36] Cottrell AH, Bilby BA. Dislocation theory of yielding and strain ageing of iron. Proc Phys Soc 1949;62:49–62. https://doi.org/10.1088/0370-1298/62/1/308.

[37] Krauss G. Tempering of lath martensite in low and medium carbon steels: assessment and challenges. Steel Res Int 2017;88:1–18. https://doi.org/10.1002/srin.201700038.

[38] Kakimoto R, Koyama M, Tsuzaki K. EBSD- and ECCI-based assessments of inhomogeneous plastic strain evolution coupled with digital image correlation. ISIJ Int 2019;59:2334–42. https://doi.org/10.2355/isijinternational.ISIJINT-2019-232.

[39] Allain-Bonasso N, Wagner F, Berbenni S, Field DP. A study of the heterogeneity of plastic deformation in IF steel by EBSD. Mater Sci Eng, A 2012;548:56–63. https://doi.org/10.1016/j.msea.2012.03.068.

[40] Reimer L. Scanning electron microscopy: physics of image formation and microanalysis. Berlin, Heidelberg: Springer; 2012. https://doi.org/10.1007/978-3-662-13562-4ISBN978-3-662-13562-4 (eBook) Library.

[41] Depover T, Pérez Escobar D, Wallaert E, Zermout Z, Verbeken K. Effect of hydrogen charging on the mechanical properties of advanced high strength steels. Int J Hydrogen Energy 2014;39:4647–56. https://doi.org/10.1016/j.ijhydene.2013.12.190.

[42] Sun Y, Cheng YF. Hydrogen permeation and distribution at a high-strength X80 steel weld under stressing conditions and the implication on pipeline failure. Int J Hydrogen Energy 2021;46:23100–12. https://doi.org/10.1016/j.ijhydene.2021.04.115.

[43] Momotani Y, Shibata A, Terada D, Tsuji N. Effect of strain rate on hydrogen embrittlement in low-carbon martensitic steel. Int J Hydrogen Energy 2017;42:3371–9. https://doi.org/10.1016/j.ijhydene.2016.09.188.

[44] Shibata A, Murata T, Takahashi H, Matsuoka T, Tsuji N. Characterization of hydrogen-related fracture behavior in as-quenched low-carbon martensitic steel and tempered medium-carbon martensitic steel. Metall Mater Trans A Phys Metall Mater Sci 2015;46:5685–96. https://doi.org/10.1007/s11661-015-3176-x.

[45] Shibata A, Yonemura T, Momotani Y, Park M heom, Takagi S, Madi Y, et al. Effects of local stress, strain, and hydrogen content on hydrogen-related fracture behavior in low-carbon martensitic steel. Acta Mater 2021;210:116828. https://doi.org/10.1016/j.actamat.2021.116828.

[46] Song Z, Li H, Wang X, Tian X, Hou H, Zhao Y. Designing grain refinement passes for multi-direction forging: a phase-field crystal study. J Mater Res Technol 2023;27:6501–12. https://doi.org/10.1016/j.jmrt.2023.10.187.

[47] Kim DH, Moallemi M, Kim KS, Cho HJ, Kim SJ. Correlation between grain size variation and hydrogen embrittlement in a cost-effective Fe40Mn40Ni10Cr10 austenitic medium entropy alloy. Int J Hydrogen Energy 2023;48:5708–17. https://doi.org/10.1016/j.ijhydene.2022.11.055.

[48] Momotani Y, Shibata A, Yonemura T, Bai Y, Tsuji N. Effect of initial dislocation density on hydrogen accumulation behavior in martensitic steel. Scripta Mater 2020;178:318–23. https://doi.org/10.1016/j.scriptamat.2019.11.051.

[49] Oriani RA. Hydrogen - the versatile embrittler. Corrosion 1987;43:390–7. https://doi.org/10.5006/1.3583875.

[50] Lynch S. Hydrogen embrittlement phenomena and mechanisms. Corrosion Rev 2012;30:105–23. https://doi.org/10.1515/corrrev-2012-0502.

[51] Robertson IM, Sofronis P, Nagao A, Martin ML, Wang S, Gross DW, et al. Hydrogen embrittlement understood. Metall Mater Trans B Process Metall Mater Process Sci 2015;46:1085–103. https://doi.org/10.1007/s11663-015-0325-y.

[52] Huang S, Zhang Y, Yang C, Hu H. Fracture strain model for hydrogen embrittlement based on hydrogen enhanced localized plasticity mechanism. Int J Hydrogen Energy 2020;45:25541–54. https://doi.org/10.1016/j.ijhydene.2020.06.271.

[53] Fazil M, Sch JC. The role of hydrogen in the edge dislocation mobility and grain boundary-dislocation interaction in a -Fe, vol. 6; 2021. https://doi.org/10.1016/j.ijhydene.2021.07.061.

[54] Michiuchi M, Nambu S, Ishimoto Y, Inoue J, Koseki T. Relationship between local deformation behavior and crystallographic features of as-quenched lath martensite during uniaxial tensile deformation. Acta Mater 2009;57:5283–91. https://doi.org/10.1016/j.actamat.2009.06.021.

[55] Mine Y, Hirashita K, Takashima H, Matsuda M, Takashima K. Micro-tension behaviour of lath martensite structures of carbon steel. Mater Sci Eng, A 2013;560:535–44. https://doi.org/10.1016/j.msea.2012.09.099.

[56] Martin ML, Fenske JA, Liu GS, Sofronis P, Robertson IM. On the formation and nature of quasi-cleavage fracture surfaces in hydrogen embrittled steels. Acta Mater 2011;59:1601–6. https://doi.org/10.1016/j.actamat.2010.11.024.

[57] Cho L, Bradley PE, Lauria DS, Martin ML, Connolly MJ, Benzing JT, et al. Characteristics and mechanisms of hydrogen-induced quasi-cleavage fracture of lath martensitic steel. Acta Mater 2021;206:116635. https://doi.org/10.1016/j.actamat.2021.116635.

[58] Lan X, Okada K, Gutierrez-Urrutia I, Shibata A. Quantitative analysis of local plasticity accompanying hydrogen-related fracture in low-carbon martensitic steel. Int J Hydrogen Energy 2023;50:333–41. https://doi.org/10.1016/j.ijhydene.2023.10.273.

[59] Okada K, Shibata A, Gong W, Tsuji N. Effect of hydrogen on evolution of deformation microstructure in low-carbon steel with ferrite microstructure. Acta Mater 2022;225:117549. https://doi.org/10.1016/j.actamat.2021.117549.